



Deep learning based breast cancer detection and classification using fuzzy merging techniques

R. Krithiga¹ · P. Geetha¹

Received: 2 August 2019 / Revised: 24 August 2020 / Accepted: 26 August 2020
© Springer-Verlag GmbH Germany, part of Springer Nature 2020

Abstract

Automatic identification of abnormal and normal cells is a critical step in computer-assisted pathology, owing to certain heterogeneous characteristics of cancer cells. However, automated nuclei detection is problematic in unevenly shaped, overlapping and touching nuclei. It is, consequently, essential to detect single and overlapping nuclei and distinguish them from single ones for a reasonable quantitative analysis. Diagnosis is improved by introducing a computer-aided diagnosis system to automatically detect breast cancer tissue nuclei from whole slide images of hematoxylin and eosin stains. We propose a method for the automatic cell nuclei detection, segmentation, and classification of breast cancer using a deep convolutional neural network (Deep-CNN) approach. The main contribution of this work is the detection of nuclei using anisotropic diffusion in a filter and applying a novel multilevel saliency nuclei detection model in ductal carcinoma of breast cancer tissue. The detected nuclei are classified into benign and malignant cells by applying the new Deep-CNN model. Finally, the novel multilevel saliency nuclei detection technique is integrated with the Deep-CNN to produce an nMSDeep-CNN model that turns out to be the most accurate results with very less computation time. The accuracy, sensitivity and specificity of the proposed system are 98.62%, 0.947 and 0.964, respectively. The classification for benign and malignant cells is evaluated by applying 10 fold cross-validation. Thus, the system can be clinically used for an objective, accurate, and rapid diagnosis of abnormal tissue. The effectiveness of the suggested framework is demonstrated through experiments on several datasets.

Keywords Breast cancer · Saliency detection · Nuclei segmentation · Anisotropic diffusion · Convolutional neural network · Deep learning

1 Introduction

Cancer causes an array of health problems in the human body, culminating in early death. A majority of new cases of breast, prostate, lung, and colon cancers can be predicted. Breast cancer, the most common cancer in women, is also the principal cause of death from cancers in women. Cancer is curable if detected early and increases the survivor's life span of people [34,57]. The breast cancer fatality rate has been rising every year. The World Health Organization's International Agency for Research on Cancer (IARC) reported an anticipated increase in the number of breast cancer cases to

1.1 million by 2030, with the gap between developed and developing nations expected to widen. Diagnostic tests are also used to gather adequate information on cancer so as to guide decisions about treatment.

According to the World Health Organization (WHO), the current diagnostic screening protocol consists of a mammography to identify suspicious regions of the breast, followed by a biopsy of potentially cancerous areas [5,18]. Till the 1990s, the analysis of medical images was limited by computational resources and medical imaging diagnostic tests that examined the structure of histological images. Generally, CAD systems scale down the workload of pathologists with contributions in the form of an efficient diagnostic process, fewer physicians, and reduced costs. To this end, there often is an attempt to replicate physicians' methods, as in, for instance, by viewing an analysis of nuclei morphology as being adequate enough to classify tissue as benign or malignant [53].

✉ R. Krithiga
rkrithigarajesh@gmail.com

P. Geetha
geethaplanisamy@gmail.com

¹ Department of Computer Science and Engineering, College of Engineering, Anna University, Guindy, Chennai, India

Breast biopsy, ultrasound, mammography, thermography, and fine-needle aspiration (FNA) cytology are a few practical means of disease diagnosis. Despite advancements in medicine, histopathological image analysis remains the most widely used method of breast cancer diagnosis. These images, generally handled by histopathologists, provide a clear diagnosis of specific cancers. The diagnosis is based on an examination of cells and tissue removed from suspicious ‘lumps and bumps’ in the infected person. Lim et al. [29] described microscopic images of tissue samples that were examined to study manifestations of the disease. Reagents that bind to specific proteins are called stains and are used to increase the contrast between different structures for a manual examination. By far, the most commonly used staining scheme is a combination of hematoxylin and eosin (H&E) [13]. Hematoxylin is a bluish-purple basophilic dye that binds strongly to the nuclei, while eosin is a red-pink stain that binds primarily to hydrophilic proteins in the cytoplasm and stromal matrix. The H&E stain dyes the deoxyribonucleic acid (DNA)-rich cell nuclei blue and the collagen-rich extracellular matrix (ECM) pink, allowing for the differentiation of nuclei-containing DNA from the surrounding ECM. The FNAC has been established as a rapid, safe, and reliable cost-effective breast cancer diagnosis method [6,42,48].

H&E-stained slides are mainly used in breast cancer analysis. The early detection of breast cancer helps in its successful treatment. Lesions play a critical role in disease diagnosis, and histopathological images help pathologists determine two types of lesions, benign and malignant. Benign lesions, though not cancerous, look abnormal. Malignant lesions, on the other hand, are cancerous, and comprise cells that divide abnormally and grow irregularly. The main challenge lies in the complex process of analyzing microscopic images manually, owing to the irregular appearance of benign and malignant cells. Further, differentiating between the nuclei and cytoplasm in the samples is a difficult process. Similarly, the overlapping segmentation of cells in cancer cell images further complicates the process, all of which create problems for pathologists. To overcome these difficulties, our work concentrates on detecting breast cancer, based on signal and overlapping nuclei, and these nuclei regions are classified into benign and malignant cells.

Automatic breast cancer detection and diagnosis methods presented in the related work in Sect. 2 are based on image processing techniques [6] to achieve nuclear segmentation and classification, which is a key module in computational pathology. Nuclear morphometric and appearance features such as density, nucleus-to-cytoplasm ratio, average size, gland shapes, mitotic counting, and detection help assess varying grades of cancer and predict effective treatment [52,56]. In this study, we have focused on the fuzzy-based statistical region-merging algorithm, which is a fast and robust method to segment an image into regions of similar inten-

sity or color [35]. It works based on the one region per pixel and then applies a statistical test for the following regions in the images, whereas the mean intensities are merged by applying the fuzzy rules. This algorithm is very efficient in solving the performance of noise corruption. Wulandari et al. [59] processed data using statistical region-merging (SRM) segmentation method and classified it using the convolutional neural network (CNN) methods. Bajger et al. [3] used statistical region merging for segmentation (SRM) in detecting mammographic masses and linear discriminant analysis (LDA) for classifying them.

In recent years, deep learning model plays an important role in the development of medical research. It is especially used in detection and classification of cancer images because it outrivals at tasks with large and also with complex training datasets, such as WSI [25,67]. The algorithms like convolutional neural networks (CNNs) have become significant advances in the domain of deep learning. One of the main diagnostic studies of breast cancer is performed using convolutional neural network. It provides both feature extraction and classification with its end-to-end learning architecture and also with its high performance in terms of computational time and accuracy in a variety of images. The advantage of the deep learning model is it is easily applicable to high dimension of data [7,36,46]. In this study, the deep-convolutional neural network (Deep-CNN) structure was used as a binary classifier to determine whether the individual's images are benign or malignant.

In this paper, a novel method to detect and classify cell nuclei from histopathology images is proposed. The contributions of the work are explained below:

- Image enhancement using anisotropic diffusion in filter, which is used for enhancing a noisy image and preserving edges to a higher extent.
- Reinforcing segmentation accuracy performance using a novel multilevel saliency nuclei detection (nMSND) technique to detect regions of interest, along with fuzzy-based statistical region merging to segment the regions. The results clearly show both single and overlapping nuclei regions.
- A design of Deep-CNN classification model to extract features from the segmented image and integration of the nMSND and Deep-CNN to produce the novel multilevel saliency deep-CNN (nMSDeep-CNN) method that classifies benign and malignant cell images much more accurately.
- The experiments are tested for nuclei detection and classification with different publicly available and benchmark datasets.
- Semi-supervised data are randomly taken from H&E-stained images and assigned to the training phase. The sample image sizes used are stretchable.

The rest of this paper is formulated as follows: Sect. 2 provides the related work. Section 3 discusses the background of the study of the model. Section 4 validates the proposed model which can accurately detect and segment nuclei regions in the samples and describe the details of the methods. Section 5 discusses feature extraction and classification. Section 6 presents the demonstration of our experimental setup, Performance evaluation, and discussion. Finally, Section 7 presents the conclusion.

2 Related work

A vast amount of literature is available for the breast cytoplasm and nucleus splitting, which includes the widely used morphological operation [60], marker-controlled watershed segmentation [49], active contours [26], Gaussian mixture models [44], statistical region merging [35], and adaptive thresholding [28]. While these methods are efficient in terms of computation complexity, they only address simple issues. The automated segmentation of cells from images is a necessary and fundamental step in cellular morphology that is critical to breast cancer diagnosis and prediction. Cell detection and segmentation are usually based on the features of the nucleus, which are distinct in different types of cells. The manual segmentation of cells in medical imaging is a labor-intensive and time-consuming task, which limits the number of cases that can be processed at a time [31,45].

To overcome this difficulty, Wan et al. [54] applied a combination of pixel, object, and semantic multilevel features that are extracted to quantitatively characterize morphological patterns and interpretable concepts from breast cancer tissue images. Wienert et al. [58] presented a novel contour-based “minimum-model” cell detection and segmentation approach that uses essential information and detects contours, independent of their shape. This approach avoids a segmentation bias with respect to shape features and yields accurate segmentation precision of 50.9% and recall of 53.859%. Wan et al. [39] used a detection framework estimate that is a nuclei saliency map, using tensor voting, followed by boundary extraction of the nuclei on the saliency map and a loopy backpropagation (LBP) algorithm on a Markov random field (MRF). These methods were tested on both whole-slide images and frames of breast cancer histopathology images. Sarkar et al. [47] introduced a novel saliency-based sparse coding and dictionary learning method to compute image similarity between a pair of images. The method leverages a salient object detection technique to obtain prominent features from images. Kapoor et al. [24] formulated a rule-based system that uses a set of fuzzy features to mark out the salient region in an image. Veta et al. [52] proposed a segmentation method for cells, based on a marker-controlled watershed segmentation

at multiple scales and with different markers, which gives accurate results.

Saliency detection, aimed at highlighting visually salient regions or objects in an image, has been a fundamental problem that has drawn extensive attention in recent years. Hamouda et al. [17] introduced a robust breast cancer prediction and diagnosis system based on the rough set (RS) and a robust classification process based on new and more effective attributes. Zhao et al. [64] discussed a saliency detection multicontext model which uses deep convolutional neural networks. Global and local contexts are utilized and integrated into a unified multicontext deep learning framework for saliency detection. The performance of the proposed approach is compared and evaluated with the clinical radial basis function and artificial neural network classification scheme. Jiao et al. [23] applied an orientation feature that is replaced by edge and corner features extracted by a linear structure tensor. Thereafter, these features are used to generate a contour activation map, and all the activation maps are directly combined into a saliency map. Peikari et al. [40] investigated the possibility of using clustering analysis to identify the underlying structure of the data space for SSL. A cluster label method was proposed to identify high-density regions in the data space, which were then used to help a supervised SVM find the decision boundary. Chen et al. [12] introduced a deep contour-aware network model under a unified multitask learning framework for more accurate detection and segmentation with end-to-end fully convolutional networks. Pan et al. [37] applied a gradient descent method to iteratively modify an input image, based on pixelwise gradients, to reduce a cost function measuring the class-specific objective of the image. The pixel-wise gradients can be efficiently computed using the backpropagation algorithm. Zheng et al. [65] proposed a hybrid of the K-means and support vector machine (K-SVM) algorithms to extract useful features and classify nuclei based on morphological feature in the H&E-stained images.

Deep learning-based approaches have developed rapidly in recent years, essentially in image classification. Convolutional neural networks (CNNs) have made breakthroughs in computer vision possible, specifically in image classification, achieving promising results that outperform the best traditional machine learning methods [36]. Guo et al. [16] designed a hybrid convolutional neural network (CNN) architectural framework, based on GoogLeNet, that merges key information to help with decision making. Bayramoglu et al. [7] developed two different models: a single-task CNN to predict malignancy and a multitask CNN to predict, simultaneously, both malignancy and image magnification levels. Yunbi et al. [30] proposed a pixel classifier, termed the fully convolutional DenseNet (FC-DenseNet), that mitigates issues with uncertainty to facilitate robust prediction during manual delineation. Deniz et al. [14] used both transfer

learning and deep feature extraction methods and adapted a pre-trained CNN model. AlexNet and Vgg16 models are considered for feature extraction, and AlexNet is used for further fine-tuning but the results were not that much better. Rezaeilouyeh et al. [46] developed a framework for breast cancer detection and prostate Gleason grading using CNN trained on images along with the magnitude and phase of shearlet coefficients.

Zhou et al. [66] proposed a novel instance relation network (IRNet) for overlapping cell segmentation and tested it on a cervical Pap smear (CPS) dataset. Alom et al. [1] proposed a recurrent convolutional neural network (RCNN) based on the U-Net, as well as a recurrent residual convolutional neural network (RRCNN) based on U-Net models, named the RU-Net and R2U-Net. Mahbod et al. [32] carried out semantic segmentation using a UNet for classification to separate the nuclei from the background. A distance map of each nucleus is created using a regression U-Net, and segmentation masks are created by applying a watershed algorithm based on the distance maps. Their scheme produces an average aggregate Jaccard index of 56.87 and is limited by its relatively high GPC memory for large images, as well as computational issues [20]. Milletari et al. [33] proposed an extension to the U-Net layout that incorporates ResNet-like residual blocks and a Dice loss layer, rather than the conventional cross-entropy that directly minimizes this commonly used segmentation error measure. Tokime et al. [51] advanced a modified architectural framework based on semantic segmentation networks such as the UNet, SegNet, and FCN. The results obtained are most interesting, with F1-scores ranging from 94% for the FCN to 96% for the UNet and SegNet falling neatly in between the two with 95%. Figure 1 shows the structure of the input images.

3 Background

In this section, a brief overview of the fundamental components of the proposed method is explained.

3.1 Laplacian

Laplacian is a differential operator given by the divergence in the gradient of a function on Euclidean space. It is usually denoted by the symbols $\nabla \cdot \nabla$, ∇^2 (where ∇ is the nabla operator). Similarly, the divergence of the gradient is also called the Laplacian, i.e. $(\nabla \cdot \nabla = \Delta)$

3.2 Gradient

In general, the image gradient is taken as vector field with the derivative of scalar field. Now the gradient that is taken

as vector of first derivative is defined as,

$$\nabla I(x, y) = \left[\frac{\partial I}{\partial x}(x, y) \frac{\partial I}{\partial y}(x, y) \right] \quad (1)$$

And the directional derivative along a direction vector ' v ' can then be defined as:

$$D_v(x, y) = \nabla I(x, y) \cdot V \quad (2)$$

The directional derivative equation 2 will be maximum when $V = \nabla I(x, y)$. similarly, when it is zero, it becomes orthogonal [61].

3.3 Divergence operator

The divergence of a vector field $F(x)$ at a point X_0 is defined as the limit of the ratio of the surface integral of ' F ' out of the surface of a closed volume ' V ' enclosing X_0 to the volume of ' V ', as ' V ' shrinks to zero. It is the inverse of gradient, and this is an indication of minor grayscale variation. In this approach, the red and green channels are used as vector field. The divergence is an operator, which takes in the vector-valued function to define this vector field and outputs a scalar-valued function measuring the change in density of the image at each point. It is defined as $\text{div} \cdot \vec{v} = \nabla \cdot \vec{v}$, where $\vec{v} = [\frac{\partial I}{\partial x_1} + \frac{\partial I}{\partial x_2} + \dots + \frac{\partial I}{\partial x_n}]$ and I_1, I_2, \dots are the component functions of \vec{v} .

3.4 Anisotropic diffusion technique

Perona and Malik introduce the techniques as a means to constrain the diffusion process to contiguous homogeneous regions, but not cross-region boundaries. The heat equation is thus modified to:

$$\frac{\partial I}{\partial t} = c(x, y, t) \nabla I + \nabla c \cdot \nabla I \quad (3)$$

where c is the function which controls the rate of diffusion at any point in the image. Generally, anisotropic diffusion can be used to remove noise from the digital images without blurring edges with a constant diffusion coefficient. The anisotropic diffusion filter reduces to the equation which is equivalent to Gaussian blurring. Hence, the edges can be used while removing noise from the images [62]. It is one of the image enhancement techniques.

4 Methodology

The proposed method provides an automatic system for nuclei detection and classification from H&E-stained images. Figure 2 depicts the overall architecture of the breast cancer

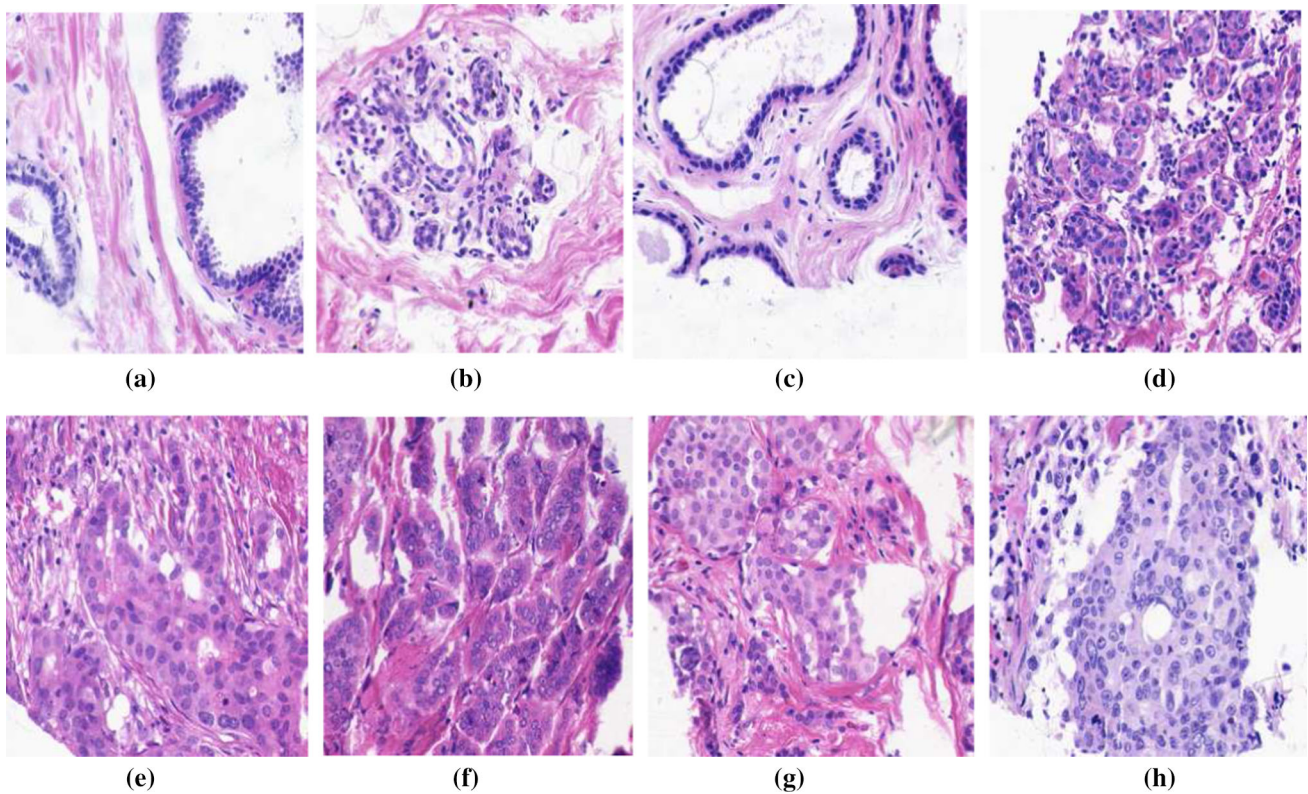


Fig. 1 Illustration of microvessels in H&E-stained histopathology images: **a–d** benign cases, and **e–h** malignant cases

prediction, which includes several steps such as biomedical data preprocessing, nuclei detection, segmentation, feature extraction, and classification. Basic methods such as the following are adopted to design the proposed system, with each described in the sections below.

4.1 Preprocessing

As a general rule, preprocessing increases the consistency of visual analysis of individual image details and enables faster and easier evaluation. The illustrations are used to generate mask images of the same resolution as in the original slides. By applying an anisotropic diffusion in a filter for a clearer and more enhanced image from the original images [19,27,41]. The gradient of an image measures how it changes and provides two pieces of information. The magnitude of the gradient tells us how quickly the image is changing, while the direction of the gradient tells us the direction in which the image is changing most rapidly. It is also known to smooth images, preserve strong edges, and enhance the contrast of the edges.

Let ' M ' denote the gradient magnitude, ' D ' represent the direction, and ' K ' be the mean grayscale image. We form the gradient vector by combining the partial derivative of the image in the x -direction and the y -direction and written as

$$M_x = \begin{bmatrix} -1 & 0 & 1 \\ -2 & 0 & 2 \\ -1 & 0 & 1 \end{bmatrix} * K \quad (4)$$

$$M_y = \begin{bmatrix} -1 & -2 & -1 \\ 0 & 0 & 0 \\ 1 & 2 & 1 \end{bmatrix} * K \quad (5)$$

$$M = \sqrt{M_x^2 + M_y^2} \quad (6)$$

$$M_1 = \tan^{-1}(M) \quad (7)$$

where M_x denotes horizontal gradient images and M_y vertical gradient images which are defined in Equations 1 and 2. The gradient computation denotes M_1 as orientation and weight.

4.2 Novel multilevel saliency-based nuclei detection (n-MSND)

In this section, a proposed novel multilevel saliency-based nuclei detection (n-MSND) model is explained. First, multilevel region detection is performed on the preprocessed image. For each scale, the seed point is calculated, based on the global color seed point and texture of the particular point. Global color seed point is obtained by,

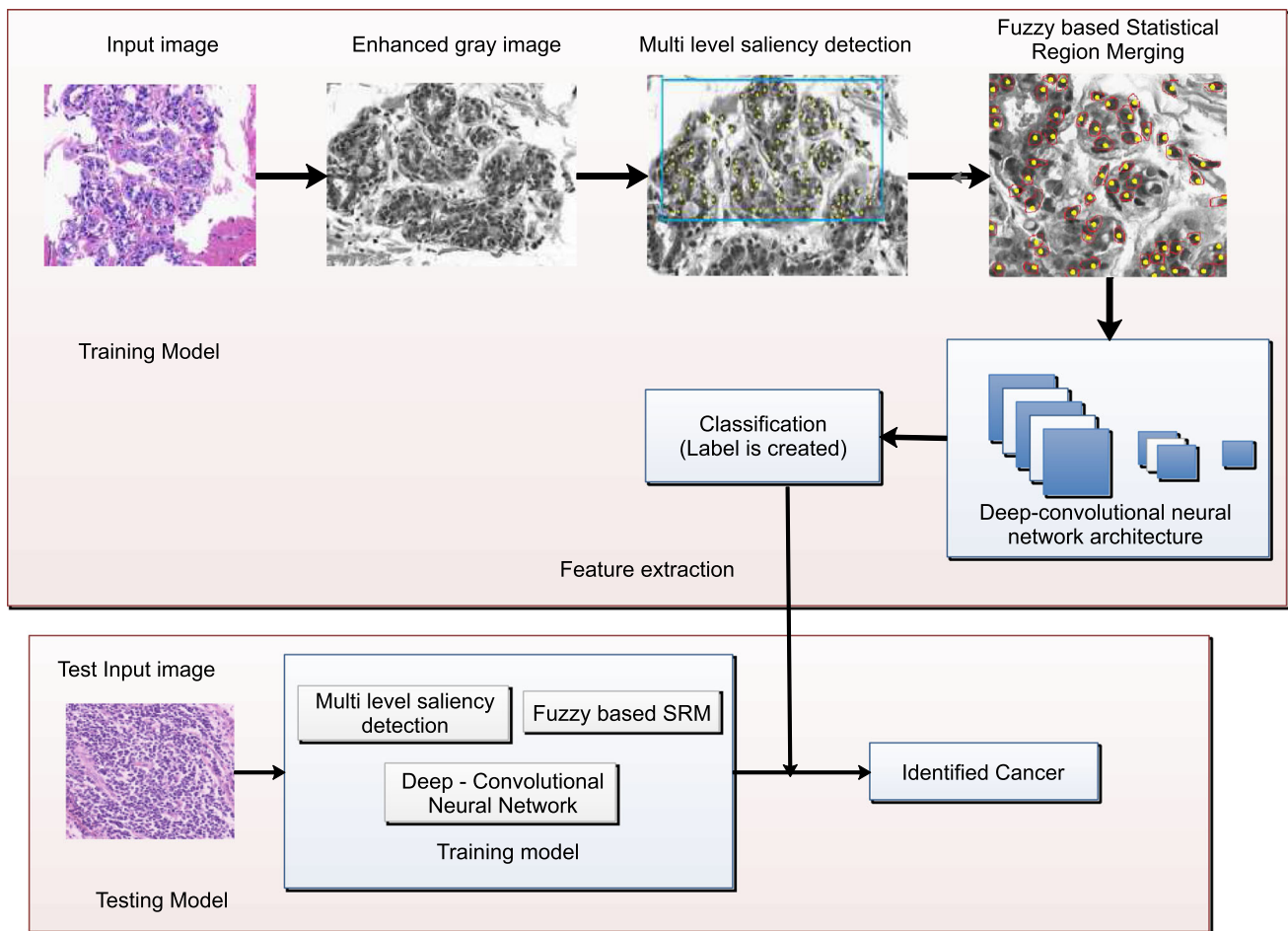


Fig. 2 Block diagram of the proposed system

- Partitioning the preprocessed image into superpixels.
- Measuring the boundary connectivity of each superpixel so as to construct the background template.

A saliency point is created through the sparse reconstruction error which is compared with the error contrast of the background template. It is a process that demonstrates the unique quality of each pixel. The goal of the process is to simplify and transform an image into something that is meaningful and easy to analyze. Detection is typically used to locate objects and boundaries in images. It is the process of assigning a label to every pixel in an image such that pixels with the same label share certain characteristics. The distance from each pixel to the remaining pixels in the same image is calculated as:

$$SD(x_k) = \sum_{i=1}^N |x_k - x_i| \quad (8)$$

where N denotes the total number of pixels in the current images. This equation can be rewritten as,

$$SD(x_k) = \sum F_n \times |x_k - x_i| \quad (9)$$

Then, the context-based error propagation is applied to further optimize the saliency point, following which the saliency detection framework is used to aggregate the superpixel-level saliency point to the pixel-level saliency point as in Equation 9.

4.2.1 Global color and texture seed point

Inspired by Wang et al. [55], we use texture prior, which is a global prior to construct the saliency point, and utilize RGB color space of H&E-stained images for segmenting the breast cancer tissue. Here, we find that the image has better contrast between abnormal and normal in the global color channel. Therefore, the blue-color component is used for further processing, which can show better detection results as other channels. The global I_C is represented as the color component of preprocessed image. Similar to the design of global saliency point based on the texture prior, extract patches are of size $m \times n$ with stride τ 1 along the image boundary and

easily obtain the average color value of each patch, which is marked as x_1, x_2, \dots, x_N , where m represents the row and n represents the column. At the same time, the average color values quantify the contribution of texture patches of the saliency point, which is used to avoid the situation that those texture patches belonging to breast cancer tissue have a great influence on the composition of the saliency point. In other words, it measures the patches located in normal tissue areas which have more weight than abnormal tissue, and the weighting ω_i for i^{th} patches satisfies the following formula:

$$\omega_i = x_i / \sum_{j=1}^N x_j, \quad i = 1, 2, \dots, N. \quad (10)$$

In the case of global color prior, when the color value of pixels is higher than the mean value of texture patches of normal tissue, then the saliency point of the pixels is zero. Hence, the following formula for the generation of the global color saliency point is denoted by I_b with i^{th} texture patch,

$$S_G(j) = \begin{cases} x_i - I_b(j), & x_i > I_b(j) \\ 0, & x_i \leq I_b(j) \end{cases} \quad (11)$$

where $j = 1, 2, \dots, N_p$, with N_p being the number of pixels in the input image, and m_i is the mean of the i^{th} texture prior patch. The final global color saliency point is accomplished by calculating the following formula:

$$S_b(j) = \sum_{i=1}^N w_i S_G(j) \quad i = 1, 2, \dots, N_p \quad (12)$$

The saliency values of normal pixels in color and texture saliency point tend to be close to zero, and the high saliency value belongs to the abnormal tissue. For the purpose of enhancing the abnormal regions, these two saliency points that utilize different pieces of information are clustered by the following strategy.

$$\text{Multilevel saliency} = x \times \text{saliency}_\alpha + y \times \text{saliency}_\beta \quad (13)$$

where x and y denote the minimum of error evaluation metric which are obtained by grid search method. In our experiments, x and y are set as 0.32 and 0.68, respectively. α and β denote global and texture points. The clustered saliency point is effective to suppress the backgrounds and enhance the objects from the experimental results.

4.2.2 Fuzzy-based statistical region merging

In this work, a fuzzy-based statistical region-merging (FSRM) algorithm for segmenting the detected area of H&E-stained

images is adopted. This method is widely used in the segmentation process on account of its efficiency, simplicity, and accurate performance without the use of quantization or color space transformations. The FSRM algorithm belongs to the family of region-merging and -growing techniques combined with geometric tests to choose the merging of the regions. The FSRM has its antecedents in an algorithm which retains arithmetical tests aimed at domain fusion [4]. The FSRM algorithm is used to evaluate pixel values within a regional area and group them, based on homogeneous properties attaining a smaller list. The key components that define this algorithm are merging (test) and the order in merging. It basically accumulates couples of adjacent pixels in the image, I , to be in a set S_I . These couples are subsequently sorted in an ascending order of a real function, $f(p, p')$, with p and p' being pixels of I and traversing this order only once. The current region to which p belongs is taken as the test. The $R(p)$ and $R(p')$ are merged if the corresponding function, f , returns true. Figure 3 illustrates the segmentation of normal and abnormal areas from a H&E-stained image, and Fig. 4 shows the results of overlapping segmentation.

Algorithm 1: Algorithm for obtaining Multilevel saliency nuclei detection and FSRM segmentation

Input : Breast cancer H&E stain images I_n (n is the total number of images)

Output: Segmented nuclei region

```

1 begin
2   Apply Anisotropic diffusion to  $x_n$  images to remove noise;
3   foreach  $I_n$  do
4     Compute the saliency detection point
5     Calculate  $S_G(j)$  as given in Equation 11
6     Measure the patch located in tissue
7     Calculate the global color saliency point
8   end
9   foreach  $x_n$  images from  $I_n$  do
10    Compute the saliency detection point
11    Calculate texture point  $S_b$  as given in Equation 12
12    Measure the patch located in tissue
13    Calculate the texture saliency point
14  end
15  Combine the two points
16  Construct the multilevel saliency nuclei detection as given
   in Equation 13
17  Apply fuzzy-based statistical region-merging (FSRM)
   method
18  Segment the location of nuclei.
19 end

```

5 Deep-CNN model for feature extraction

Convolutional neural networks are feed-forward, backpropagation neural networks with a special architecture inspired

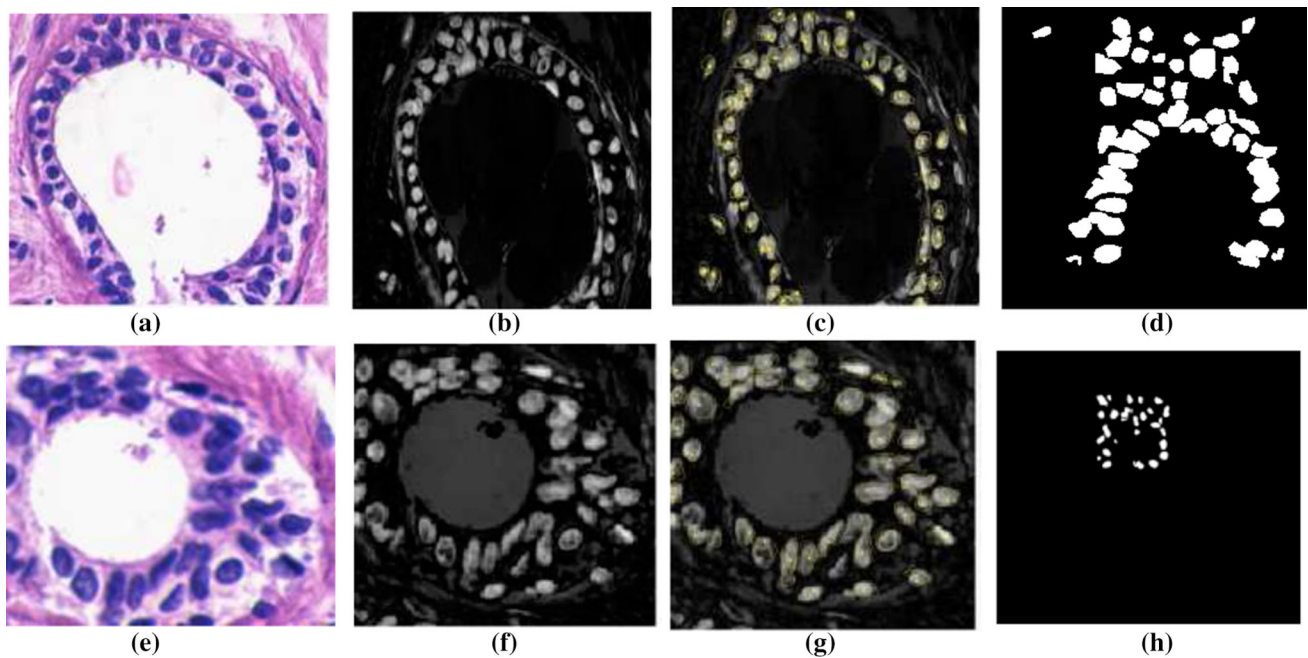


Fig. 3 Segmentation results: **a, e** are input images, **b, f** preprocessed images, **c, g** fuzzy-based statistical region-merging images (FSRM), and **d, h** are ground-truth images

by biological systems and have achieved success in image, video, audio, and artificial intelligence applications. CNNs have been used in various applications, including handwriting classification, object identification, and determination of H&E cells [22]. The Deep-CNN comprises different, alternative layers of trainable filters and neighborhood pooling operations that derive simple to complex features from input image patches. Deep-CNN layers have a nonlinear function, and it constructs high-level representations of patches from low-level information automatically. The detected image that has more meaningful features has more hidden layers. Despite the plethora of deep convolutional neural networks with similar architecture, the layers in the proposed model are appropriately modified. The Deep-CNN model designed consists of six convolutional layers, six pooling layers, one flattening vector, two fully connected layers, and two classes. Modifying the layers enhances the performance of our proposed method.

The proposed Deep-CNN architecture for classification uses preprocessed and segmented patches derived from normalized images of H&E-stained images as shown in Figs. 6 and 5, where Table 1 shows the features used in image analysis for H&E-stained image of breast cancer. This patch-driven CNN architecture is developed in order to facilitate a comparison with our novel Deep-CNN approach.

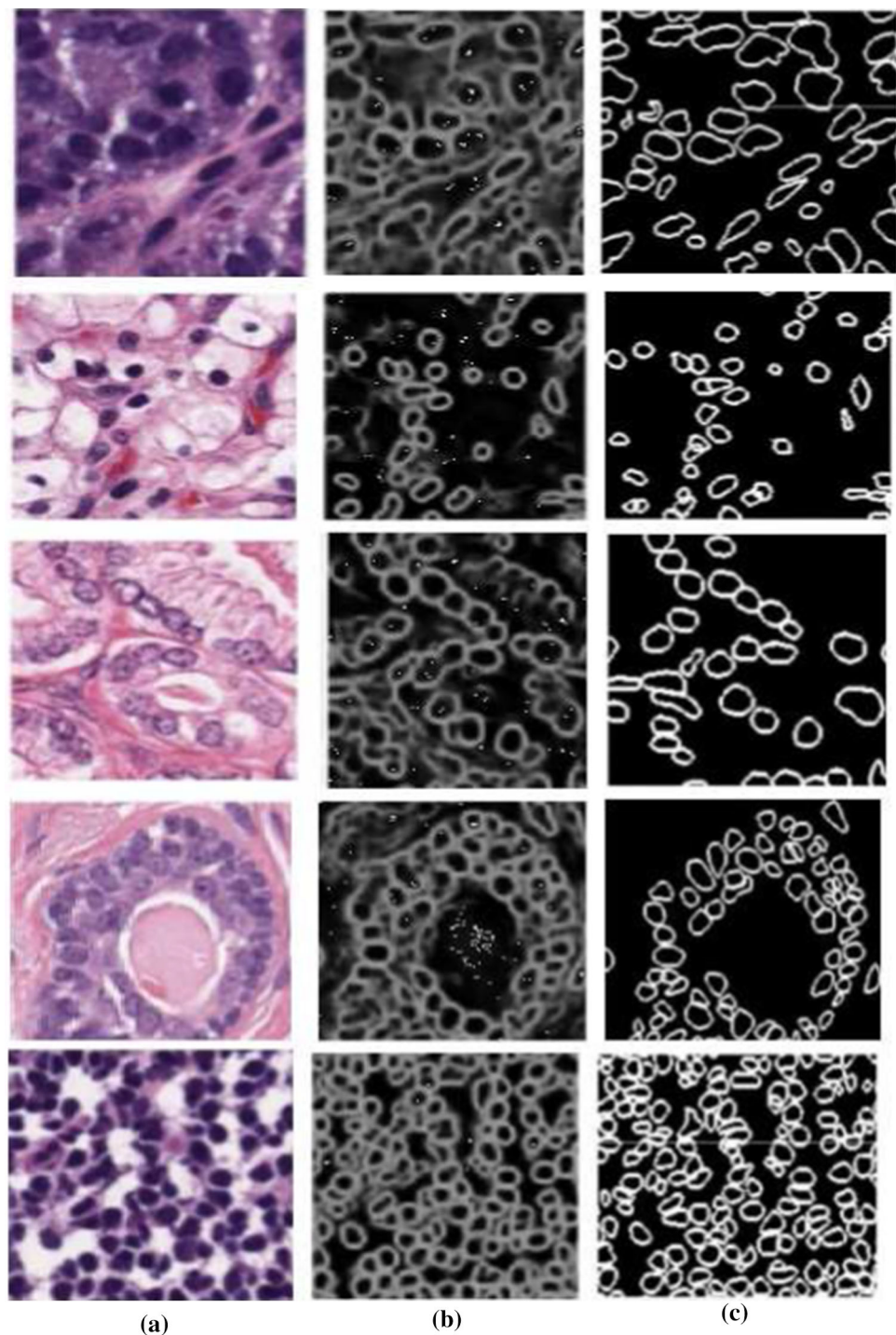
5.1 Model definition

A convolutional layer is used to learn features from images. The advantages of the CNN model are local perception and weight sharing, which are fully reflected in the convolutional layer. The size of the scan window is the same as that of the convolutional kernel, and only partial images or feature maps are scanned at a time. A feature map shares a convolutional kernel, which is convolved with a number of feature maps from the previous layer. The corresponding elements and a bias are then added. Finally, the weighted sum is conveyed to a nonlinear activation function to obtain a new feature map [11, 15, 63]. The activation function can be a rectified linear unit (ReLU) function or sigmoid function. The output is $f(x) = \max(0, x)$. The process of feature extraction is given as follows:

$$a_j^l = f \left(\sum_{i \in m^{(l-1)}} x_i^{(l-1)} * W_{(ij)}^{(l)} \times b_j^{(l)} \right) \quad (14)$$

In Equation 12, a_j^l denotes the j th feature map of the l th layer, $w_{(ij)}^{(l)}$ shows the weights between the j th feature map of the l th layer and the i th feature map of the $(l-1)$ th layer, $b_j^{(l)}$ represents the offset of the j th feature map in the l^{th} layer and

Fig. 4 Some segmentation results. From left to right: **a** original breast cell image, **b** preprocessed images, **c** segmentation results by the proposed methods, respectively



belongs to $m^{(l-1)}$ that indicates all feature maps in the $m^{(l-1)}$ layer. The convolutional kernel size of the CNN model is 3×3 pixels, which is beneficial for extracting the finer features from the image and reduces the amount of parameters used.

Generally, pooling layer is used to compress the feature map. Feature compression is performed to extract the main features, which reduces the size of the feature map and simplifies the network. In general, the feature map of the

convolutional layer is downsampled by taking the regional maximum or average value. All features are connected and prepared for classification. The convolutional layers can be transformed into a global convolution with the size of the previous convolutional kernel if the previous layer is the convolutional layer; otherwise, the convolutional layer is converted to a convolutional with a 1×1 convolutional kernel [43]. The final stage of CNN is the output layer, which

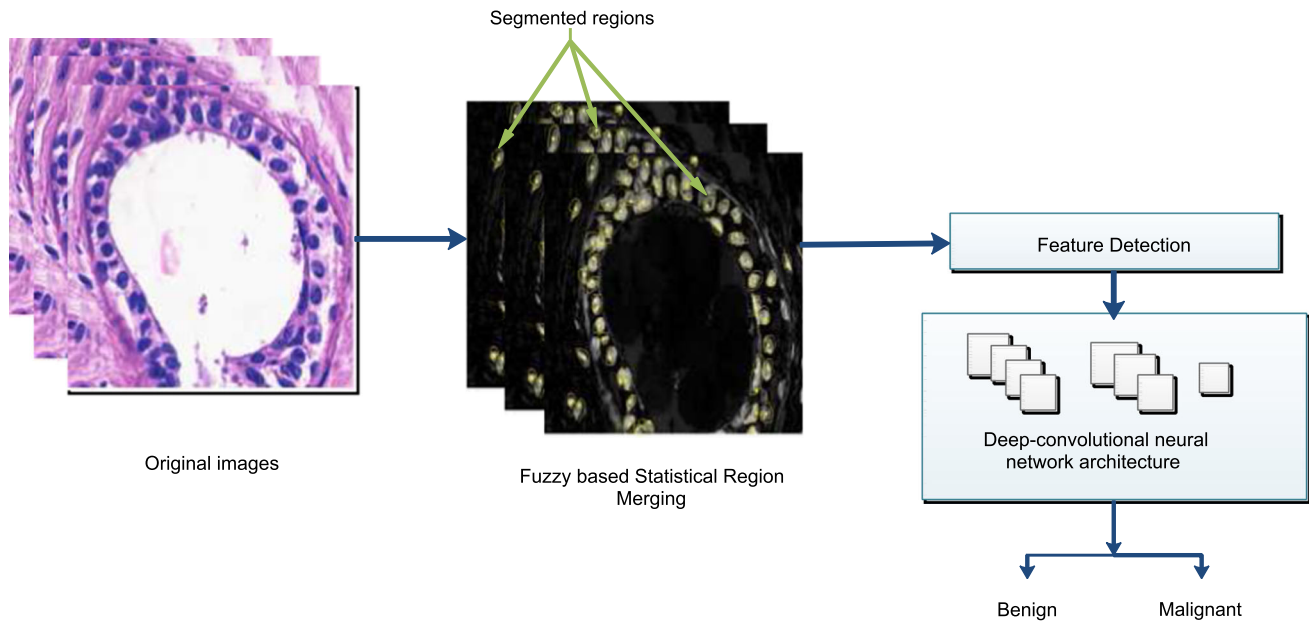


Fig. 5 Feature detection flow

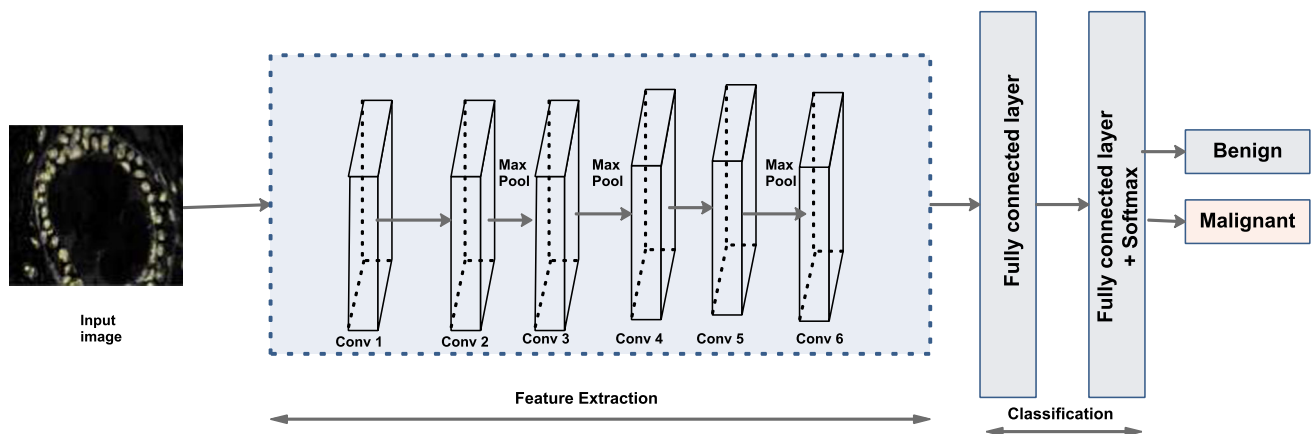


Fig. 6 Deep-CNN architecture proposed in our study

is fully connected to the previous convolutional layer. Equation 15 shows the calculation of the output layer of the j^{th} sigmoid neuron, in which l represents the output layer, N^l represents the number of sigmoid neurons, w_i , j^l shows the weights from feature vector i^{th} to the last convolution layer, b_j^l denotes the coefficient of the j^{th} neuron in layer l and f^l is the sigmoid transfer function:

$$a_j^l = f^l \left(\sum_{i=1}^{N_{l-1}} w_i j^l a_i^{(l-1)} \times b_j^l \right) \quad (15)$$

Deep-CNN produces a system output in vector form ($1 \times N$) in the output layer denoted as Y for each input datum, which can be expressed as,

$$Y = [Y_1^l, Y_2^l, \dots, Y_N^l] \quad (16)$$

The feature nodes are obtained by the final layer of the network. The output of the first layer acts as input to the second layer of the Deep-CNN model. Similarly, feature nodes act this way with all the layers. Thus, it has six CNN layers, each with 24 filters, and ending with the kernel layer used for iterations with certain values. This network contains two fully connected layers hidden with 180 nodes, which gives the output of the model. Training is required once the model is designed. The algorithm trains each node layer by layer, based on which the weights are updated and the process repeated for the other layers as well. The weights are optimized to prove the computational efficiency of the model. Finally, we leveraged semi-supervised learning

Table 1 Feature extraction using our proposed Deep-CNN approach

Layer	Kernel size	Activation	Output size
Input	3	–	$226 \times 226 \times 3$
Convolutional layer 1 (conv 1)	3×3	Relu	$226 \times 226 \times 64$
Max pooling 1	3×3	MaX	$11 \times 11 \times 25$
Convolutional layer 2 (conv 2)	3×3	Relu	$112 \times 112 \times 128$
Max pooling 2	3×3	MaX	$13 \times 13 \times 2$
Convolutional layer 3 (conv 3)	3×3	Relu	$64 \times 64 \times 128$
Max pooling 3	3×3	MaX	$11 \times 11 \times 2$
Convolutional layer 4 (conv 4)	3×3	Relu	$56 \times 56 \times 256$
Max pooling 4	3×3	MaX	$11 \times 11 \times 2$
Convolutional layer 5 (conv 5)	3×3	Relu	$27 \times 27 \times 256$
Max pooling 5	3×3	MaX	$11 \times 11 \times 2$
Convolutional layer 6 (conv 6)	3×3	Relu	$14 \times 14 \times 256$
Max pooling 6	3×3	MaX	$11 \times 11 \times 2$
Flatten	–	–	$7 \times 7 \times 256$
FC1	–	–	124
FC2+Softmax	–	–	2

method for training: that is, we improved the generalization of a baseline model by fine-tuning it with unlabeled data from other data and to verify the effectiveness of the proposed approach. Semi-supervised learning (SSL) methods are able to learn from fewer labeled data points with the help of a large number of unlabeled data points. Here, we applied an expectation–maximization (EM) algorithm to estimate the optimized parameter of the Gaussian mixtures model to train the algorithm, which is named as multilevel saliency-based EM. It shows how efficiently the model works, avoids overfitting problem, and boosts the performance too.

6 Experimental results and discussion

6.1 Dataset description

The proposed system was evaluated using histopathology examination of fine-needle aspiration samples, which are critical in all aspects ranging from cancer detection to treatment planning. The selected images were subsequently obtained using digital photography under a light microscope in a 2684×1943 -sized Tagged Image File Format (TIFF), for the BC patient group from four different benchmark datasets that has got ethical approval from everyone to carry out this research. The first dataset is collected from Indiana University Health Pathology Laboratory [21]. The second dataset local is collected from Tata Medical Center (TMC) [50]. The third benchmark dataset, collected from The Cancer Imaging Archive (TCIA), is a service that identifies and hosts huge masses of cancer medical images [10]. The fourth is the Breast Cancer Histopathological Database (BreakHis)

from the Laboratory of Vision, Robotics and Imaging (VRI) [9]. These comprised a total of 9109 microscopic images of breast tumor tissue collected from 82 patients using different magnifying factors ($40\times$, $100\times$, $200\times$, and $400\times$). To date, it contains 2480 benign and 5429 malignant samples (700×460 pixels, three-channel RGB, eight-bit depth in each channel, PNG format).

6.2 Experimental design

The implementation was done under MATLAB R2018a platform and Python 2.7 and executed on a machine with a 3.40 GHz Intel Core i5-7500 CPU and 16GB RAM. The Deep-CNN models were designed and implemented on the deep learning framework Pytorch package using NVIDIA GeForce GTX TITAN X with 12 GB RAM. Comparison was carried out between our proposed method and state-of-the-art methods. The dataset is composed of an extended set of 449 images and a separate test set of 320 images. In these datasets, the two classes are balanced. The images were selected; using this, the pathology classification can be determined based on the image contents. An additional test set of 180 images is provided with image of increased ambiguity, which is denoted as ‘extended’ dataset.

6.3 Performance evaluation

The performance of the proposed algorithm is evaluated based on the following measures: accuracy, Mathews correlation coefficient (MCC), F1-score, precision, sensitivity, and specificity. Here, α is the number of true predictions that an occurrence is true, μ is the number of false predictions that

Table 2 Definition of the abbreviation

	Actual diagnosis		Total
	Benign	Malignant	
<i>Prediction outcome</i>			
Benign	α	μ	$\alpha + \mu$
Malignant	ϕ	β	$\phi + \beta$
Total	$\alpha + \phi$	$\mu + \beta$	N

an occurrence is true, ϕ is the number of true predictions that an occurrence is false, β is the number of false predictions that an occurrence is false.

6.3.1 Accuracy (φ)

Accuracy determines how the classifier is predicting the classes. It measures the effectiveness of the classifiers. Typically, error rate is inversely proportional to accuracy:

$$\varphi = \frac{\alpha + \beta}{\alpha + \beta + \phi + \mu} \quad (17)$$

6.3.2 Precision (γ)

Precision refers to the ratio of labeled nuclei that are separated by the algorithm. The precision helps in measuring the effectiveness of the algorithm in detecting relevant nuclei regions. Precision is defined as rate of γ . It is a measure of predicted class that is correctly detected:

$$\gamma = \frac{\alpha}{\alpha + \phi} \quad (18)$$

6.3.3 Sensitivity (λ)

For cancer diagnosis, a good recall value is more important than the precision. Sensitivity is also defined as rate of λ . It is a measure of class which is incorrectly detected:

$$\lambda = \frac{\alpha}{\alpha + \mu} \quad (19)$$

6.3.4 Specificity (δ)

Specificity refers to the proportion of time that a test yields true negative. Specificity is also defined as rate of δ :

$$\delta = \frac{\mu}{\mu + \phi} \quad (20)$$

6.3.5 F1-score (F_1)

F1-measure is a harmonic mean of precision and recall. This metric will be a hypothesis for accuracy. The definitions are

as follows:

$$F_1 = 2 * \frac{\delta * \lambda}{\delta + \lambda} \quad (21)$$

6.3.6 Matthews correlation coefficient (MCC)

MCC is used to measure the binary classifier. Its value ranges between -1 and $+1$, where -1 , $+1$, and 0 correspond to worst, best, and random predictions, respectively:

$$\text{MCC} = \frac{(\alpha * \phi) - (\mu * \beta)}{\sqrt{(\alpha + \mu)(\alpha + \phi)(\phi + \beta)(\phi + \mu)}} \quad (22)$$

6.3.7 Intersection over union (IoU)

The intersection over union (IoU), also known as the Jaccard Index, is one of the most commonly used metrics. IoU is the area of overlap (AO) between the predicted segmentation and the ground truth divided by the area of union (AU) between the predicted segmentation and the ground-truth images:

$$\text{IoU} = \frac{\text{AO}}{\text{AU}} \quad (23)$$

Finally, results are cross-validated by applying the free-response receiver operating curve (FROC), and for binary classification problem, we used area under curve (AUC) score, which is defined as the area under ROC curve. The main reason for evaluating the ROC is the positive and negative samples keep changing in test set but ROC remains unchanged.

6.3.8 Analytical ablation study

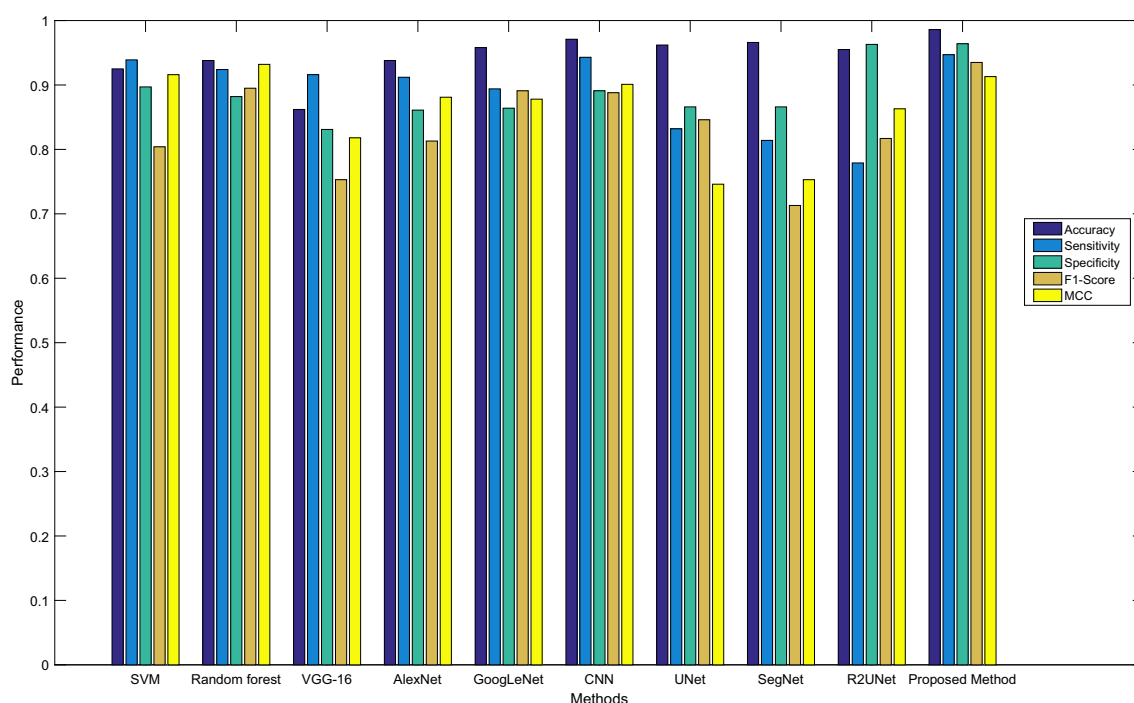
We conducted an ablation study to show the overall performances of our proposed method (nMSDeep-CNN) in each component: (i) the nMSND without data augmentation (AD), (ii) the nMSND with data augmentation (nMSND +AD), and (iii) proposed method (nMSDeep-CNN). The results are shown in Table 6. In the model, AD refers to the semi-supervised learning technique. Here, used a multi-level saliency-based expectation-maximization algorithm in the study. Furthermore, the evaluation is conducted across all four datasets. Our findings showed that the proposed nMSDeep-CNN model performs better than other models, with an average F1-score of 0.963 and an average IOU of 0.861.

6.4 Discussion

In this section, a comprehensive evaluation and a qualitative assessment of the proposed model are presented below. First, a raw RGB image is taken as an input image for the model.

Table 3 Comparison between the other methods and our proposed method

Classifiers	Accuracy	Sensitivity	Specificity	F1-score	MCC	AUC
Support vector machine (SVM)	0.925	0.939	0.897	0.804	0.916	84.3
Random forest classifier	0.936	0.924	0.882	0.895	0.932	86.8
VGG-16	0.862	0.916	0.831	0.753	0.818	90.4
AlexNet	0.938	0.912	0.861	0.813	0.881	89.3
Stacked sparse autoencoder (SSAE)	0.928	0.894	0.873	0.901	0.925	94.5
GoogLeNet	0.958	0.894	0.864	0.891	0.878	88.2
Convolutional neural network (CNN)	0.971	0.943	0.891	0.888	0.901	97.3
UNET	0.962	0.832	0.866	0.846	0.746	96.4
SegNet	0.966	0.814	0.866	0.713	0.754	95.7
R2U-Net	0.955	0.779	0.893	0.817	0.863	94.9
Proposed method	0.986	0.947	0.964	0.935	0.913	99.4

**Fig. 7** Performance comparison between the state-of-the-art methods and the proposed method

It is preprocessed and segmented, using the novel multi-level saliency nuclei detection approach discussed in Sect. 4. Finally, the Deep-CNN model is trained to learn benign and malignant nuclei features from all types of images. The Deep-CNN model is employed on different datasets as well. The results obtained using the novel multilevel saliency detection algorithm prove the method to be most efficient, as the detection rates increased and classification results were accurately obtained.

Compared with state-of-the-art methods, our proposed work gets more optimal results in terms of accuracy, sen-

sitivity, specificity, and AUC of 0.986, 0.947, 0.964 and 99.4 as shown in Table 3. Table 4 compares the results of our proposed method in terms of accuracy, F1-score, sensitivity, specificity, and precision with those of six other methods in different datasets. Similarly, Table 7 shows the 5 fold and 10 fold cross-validation accuracy performed with all features, with the main feature selected recorded in the evaluation. Validation of nMSDeep-CNN model is demonstrated and evaluated by means of ablation study, and the results are shown in Table 6. Finally, Table 5 explains the classification of our proposed method with four different datasets.

Table 4 Comparison of the proposed model with different datasets

Datasets	Method	ACC	Sn	Sp	PPV	MCC	F1-score	AUC	FROC
TCIA	DCN [38]	0.924	0.883	0.915	0.907	0.894	0.839	95.3	82.1
	DBN-MCS [8]	0.906	0.937	0.894	0.625	0.811	0.753	89.1	74.3
	FC-DenseNet [30]	0.852	0.863	0.838	0.784	0.794	0.827	88.1	72.3
	3-CNN [63]	0.967	0.923	0.949	0.896	0.931	0.951	98.1	83.1
	CNN+SVM [2]	0.778	0.916	0.897	0.863	0.864	0.921	85.8	76.3
	IRNET [66]	0.881	0.912	0.841	0.863	0.813	0.751	89.2	78.3
	Proposed method	0.986	0.945	0.966	0.913	0.908	0.962	99.2	85.1
BreakHis	DCN [38]	0.919	0.879	0.912	0.904	0.899	0.842	95.8	82.4
	DBN-MCS [8]	0.902	0.935	0.891	0.63	0.819	0.743	90.5	78.2
	FC-DenseNet [30]	0.848	0.862	0.832	0.792	0.798	0.822	88.6	72.4
	3-CNN [63]	0.956	0.918	0.951	0.901	0.932	0.953	98.3	83.4
	CNN+SVM [2]	0.773	0.918	0.894	0.861	0.869	0.927	86.1	76.9
	IRNET [66]	0.889	0.921	0.851	0.874	0.819	0.754	89.7	79.1
	Proposed method	0.988	0.947	0.964	0.909	0.910	0.967	99.4	86.3
TMC	DCN [38]	0.914	0.889	0.913	0.901	0.897	0.835	95.2	81.9
	DBN-MCS [8]	0.90	0.932	0.896	0.667	0.816	0.752	90.2	77.4
	FC-DenseNet [30]	0.851	0.861	0.847	0.801	0.795	0.829	88.4	72.2
	3-CNN [63]	0.961	0.929	0.947	0.894	0.931	0.952	98.2	83.2
	CNN+SVM [2]	0.771	0.916	0.897	0.869	0.865	0.925	85.9	76.2
	IRNET [66]	0.883	0.916	0.849	0.868	0.814	0.753	89.4	78.2
	Proposed method	0.988	0.947	0.966	0.904	0.908	0.965	99.3	85.3
IUHPL	DCN [38]	0.912	0.885	0.918	0.89	0.895	0.829	95.6	82.1
	DBN-MCS [8]	0.905	0.932	0.894	0.641	0.815	0.746	90.2	77.1
	FC-DenseNet [30]	0.849	0.867	0.839	0.783	0.794	0.834	88.3	72.2
	3-CNN [63]	0.965	0.924	0.944	0.895	0.932	0.952	98.2	83.2
	CNN+SVM [2]	0.778	0.917	0.892	0.869	0.866	0.929	85.8	76.3
	IRNET [66]	0.885	0.917	0.849	0.869	0.812	0.752	89.1	78.4
	Proposed method	0.983	0.946	0.962	0.911	0.914	0.961	99.3	85.3

Acc accuracy, *Sn* sensitivity, *Sp* specificity, *PPV* positive predictive values, *MCC* Matthews correlation coefficient, *AUC* area under the curve, *FROC* Free-response Receiver Operating Characteristic

As per Algorithm 1, the time complexity of nuclei detection is approximately order of $\approx O(n^2)$. The principal advantages of the proposed system are: (i) The model is fully automatic and works independently, (ii) System accuracy is high when compared to other state-of-the-art methods, (iii) Our proposed method has achieved better in overlapping cell segmentation with high precision value, (iv) Computation time is very fast and the prediction rates show that the model outperforms others, and (v) The proposed method offers a considerably good performance across our datasets. The limitation of our proposed method is that only binary classification is processed and will be overcome in our future works.

7 Conclusion

This paper has proposed a fast and refined cancer nuclei region detection. The classification framework in H&E-

Table 5 Comparison results of the proposed method

Dataset	AUC	FROC	MCC
TCIA dataset [10]	99.1	85.1	0.908
BreakHis [9]	99.4	86.3	0.910
TMC [50]	99.1	85.3	0.908
IUHPL [21]	99.2	85.3	0.914

stained breast cancer images classifies cancer into two classes of lesions, benign and malignant. We have designed a screening process to detect nuclei using a novel multilevel saliency nuclei detection algorithm that offers efficient results. By tuning the feature from segmented image, it is moved to future classification using Deep-CNN architecture, which is more faster and accurate. Our approach, with 98.62% mean accuracy, has proved most satisfactory. It is hoped that it can be used as an efficient framework to develop diagnostic tools

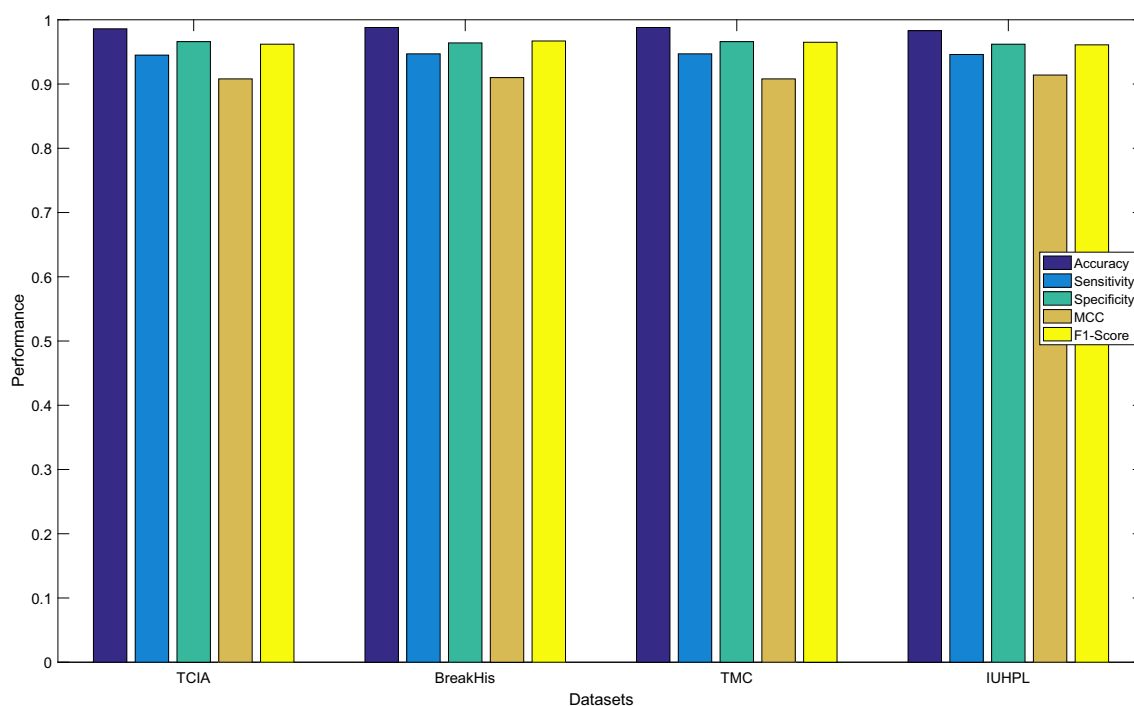


Fig. 8 Comparison between different datasets and the proposed method

Table 6 Ablation studies of nMSDeep-CNN model

Methods	TCIA dataset		BreakHis dataset	
	F1-score	IoU	F1-score	IoU
nMSND	0.953	0.825	0.957	0.82
nMSND + AD	0.959	0.846	0.959	0.842
nMSND + AD + nMSDeep-CNN	0.962	0.861	0.964	0.859
Methods	TMC dataset		IUHPL dataset	
	F1-score	IoU	F1-score	IoU
nMSND	0.954	0.828	0.952	0.827
nMSND + AD	0.956	0.841	0.959	0.849
nMSND + AD + nMSDeep-CNN	0.965	0.864	0.961	0.863

Table 7 Comparison of cross-validation accuracy

Method	$K = 10$	$K = 5$
VGG-16	0.918	0.893
AlexNet	0.938	0.914
GoogLeNet	0.958	0.931
SegNet	0.966	0.948
Proposed method	0.986	0.934

that assist clinicians and pathologists in the rapid evaluation of the tumorous lesions screened. Further, it is used for other types of stained images as well.

Compliance with ethical standards

Conflict of interest The authors declare that they have no conflict of interest.

Ethical approval This article does not contain any studies with human participants or animals performed by any of the authors.

Informed consent Informed consent was obtained from all individual participants included in the study.

References

1. Alom, M.Z., Hasan, M., Yakopcic, C., Taha, T.M., Asari, V.K.: Recurrent residual convolutional neural network based on U-

- Net (R2U-Net) for medical image segmentation. arXiv preprint [arXiv:1802.06955](https://arxiv.org/abs/1802.06955) (2018)
2. Araújo, T., Aresta, G., Castro, E., Rouco, J., Aguiar, P., Eloy, C., Polónia, A., Campilho, A.: Classification of breast cancer histology images using convolutional neural networks. *PLoS ONE* **12**(6), e0177544 (2017)
 3. Bajger, M., Ma, F., Williams, S., Bottema, M.: Mammographic mass detection with statistical region merging. In: 2010 International Conference on Digital Image Computing: Techniques and Applications, pp. 27–32. IEEE (2010)
 4. Bandhyopadhyay, S.K., Paul, T.U.: Automatic segmentation of brain tumour from multiple images of brain MRI. *Int. J. Appl. Innov. Eng. Manag. IJAEM* **2**(1), 240–8 (2013)
 5. Bargalló, X., Velasco, M., Santamaría, G., Del Amo, M., Arguis, P., Gómez, S.S.: Role of computer-aided detection in very small screening detected invasive breast cancers. *J. Digit. Imaging* **26**(3), 572–577 (2013)
 6. Bartels, D., Hanke, C., Schneider, K., Michel, D., Salamini, F.: A desiccation-related elip-like gene from the resurrection plant *Craterostigma plantagineum* is regulated by light and ABA. *EMBO J.* **11**(8), 2771–2778 (1992)
 7. Bayramoglu, N., Kannala, J., Heikkilä, J.: Deep learning for magnification independent breast cancer histopathology image classification. In: 2016 23rd International Conference on Pattern Recognition (ICPR), pp. 2440–2445. IEEE (2016)
 8. Beevi, K.S., Nair, M.S., Bindu, G.: A multi-classifier system for automatic mitosis detection in breast histopathology images using deep belief networks. *IEEE J. Transl. Eng. Health Med.* **5**, 1–11 (2017)
 9. Breast Cancer Histopathological Database. <https://web.inf.ufpr.br/vri/databases/breast-cancer-histopathological-database-breakhis/> (2017)
 10. Cancer Imaging Archive: The cancer imaging archive (TCIA). <https://www.cancerimagingarchive.net/histopathology-imaging-on-tcia> (2019)
 11. Chen, J.M., Qu, A.P., Wang, L.W., Yuan, J.P., Yang, F., Xiang, Q.M., Maskey, N., Yang, G.F., Liu, J., Li, Y.: New breast cancer prognostic factors identified by computer-aided image analysis of he stained histopathology images. *Sci. Rep.* **5**, 10690 (2015)
 12. Chen, H., Qi, X., Yu, L., Dou, Q., Qin, J., Heng, P.A.: DCAN: deep contour-aware networks for object instance segmentation from histology images. *Med. Image Anal.* **36**, 135–146 (2017)
 13. Chen, J.M., Li, Y., Xu, J., Gong, L., Wang, L.W., Liu, W.L., Liu, J.: Computer-aided prognosis on breast cancer with hematoxylin and eosin histopathology images: a review. *Tumor Biol.* **39**(3), 1010428317694550 (2017)
 14. Deniz, E., Şengür, A., Kadiroğlu, Z., Guo, Y., Bajaj, V., Budak, Ü.: Transfer learning based histopathologic image classification for breast cancer detection. *Health Inf. Sci. Syst.* **6**(1), 18 (2018)
 15. Goodfellow, I., Bengio, Y., Courville, A.: Deep learning. <http://www.deeplearningbook.org> (2016)
 16. Guo, Y., Dong, H., Song, F., Zhu, C., Liu, J.: Breast cancer histology image classification based on deep neural networks. In: International Conference Image Analysis and Recognition, pp. 827–836. Springer (2018)
 17. Hamouda, S.K.M., Wahed, M.E., Alez, R.H.A., Riad, K.: Robust breast cancer prediction system based on rough set theory at national cancer institute of Egypt. *Comput. Methods Programs Biomed.* **153**, 259–268 (2018)
 18. Hrebien, M., Steć, P., Nieczkowski, T., Obuchowicz, A.: Segmentation of breast cancer fine needle biopsy cytological images. *Int. J. Appl. Math. Comput. Sci.* **18**(2), 159–170 (2008)
 19. Hu, K., Liu, S., Zhang, Y., Cao, C., Xiao, F., Huang, W., Gao, X.: Automatic segmentation of dermoscopy images using saliency combined with adaptive thresholding based on wavelet transform. *Multimedia Tools Appl.* (2019). <https://doi.org/10.1007/s11042-019-7160-0>
 20. Ibtehaz, N., Rahman, M.S.: Multiresunet: rethinking the u-net architecture for multimodal biomedical image segmentation. *Neural Netw.* **121**, 74–87 (2020)
 21. Indiana University Health Pathology Lab. <https://iuhealth.org/pathology-lab-services> (2017)
 22. Irshad, H., Veillard, A., Roux, L., Racoceanu, D.: Methods for nuclei detection, segmentation, and classification in digital histopathology: a review current status and future potential. *IEEE Rev. Biomed. Eng.* **7**, 97–114 (2014)
 23. Jiao, Z., Gao, X., Wang, Y., Li, J.: A deep feature based framework for breast masses classification. *Neurocomputing* **197**, 221–231 (2016)
 24. Kapoor, A., Biswas, K., Hanmandlu, M.: An evolutionary learning based fuzzy theoretic approach for salient object detection. *Vis. Comput.* **33**(5), 665–685 (2017)
 25. Kaur, T., Gandhi, T.K.: Deep convolutional neural networks with transfer learning for automated brain image classification. *Mach. Vis. Appl.* **31**, 1–16 (2020)
 26. Keatmanee, C., Chaumrattanakul, U., Kotani, K., Makhanov, S.S.: Initialization of active contours for segmentation of breast cancer via fusion of ultrasound, doppler, and elasticity images. *Ultrasonics* **94**, 438–453 (2017)
 27. Kratz, A., Kettlitz, N., Hotz, I.: Particle-based anisotropic sampling for two-dimensional tensor field visualization. *Vis. Model. Vis.* (2011). <https://doi.org/10.2312/PE/VMV/VMV11/145-152>
 28. Li, G., Liu, T., Nie, J., Guo, L., Chen, J., Zhu, J., Xia, W., Mara, A., Holley, S., Wong, S.: Segmentation of touching cell nuclei using gradient flow tracking. *J. Microsc.* **231**(1), 47–58 (2008)
 29. Lim, X., Sugimoto, K., Kamata, S.I.: Nuclei detection based on secant normal voting with skipping ranges in stained histopathological images. *IEICE Trans. Inf. Syst.* **101**(2), 523–530 (2018)
 30. Liu, Y., Zhang, X., Cai, G., Chen, Y., Yun, Z., Feng, Q., Yang, W.: Automatic delineation of ribs and clavicles in chest radiographs using fully convolutional densenets. *Comput. Methods Programs Biomed.* **180**, 105014 (2019)
 31. Luo, E., Chan, S.H., Nguyen, T.Q.: Image denoising by targeted external databases. In: 2014 IEEE International Conference on Acoustics, Speech and Signal Processing (ICASSP), pp. 2450–2454. IEEE (2014)
 32. Mahbod, A., Schaefer, G., Ellinger, I., Ecker, R., Smedby, Ö., Wang, C.: A two-stage u-net algorithm for segmentation of nuclei in H&E-stained tissues. In: European Congress on Digital Pathology, pp. 75–82. Springer (2019)
 33. Milletari, F., Navab, N., Ahmadi, S.A.: V-Net: fully convolutional neural networks for volumetric medical image segmentation. In: 2016 Fourth International Conference on 3D Vision (3DV), pp. 565–571. IEEE (2016)
 34. Murakami, R., Kumita, S., Tani, H., Yoshida, T., Sugizaki, K., Kuwako, T., Kiriya, T., Hakoza, K., Okazaki, E., Yanagihara, K., et al.: Detection of breast cancer with a computer-aided detection applied to full-field digital mammography. *J. Digit. Imaging* **26**(4), 768–773 (2013)
 35. Nock, R., Nielsen, F.: Statistical region merging. *IEEE Trans. Pattern Anal. Mach. Intell.* **26**(11), 1452–1458 (2004)
 36. Oquab, M., Bottou, L., Laptev, I., Sivic, J.: Learning and transferring mid-level image representations using convolutional neural networks. In: Proceedings of the IEEE Conference on Computer Vision and Pattern Recognition, pp. 1717–1724 (2014)
 37. Pan, H., Wang, B., Jiang, H.: Deep learning for object saliency detection and image segmentation. arXiv preprint [arXiv:1505.01173](https://arxiv.org/abs/1505.01173) (2015)
 38. Pan, X., Li, L., Yang, H., Liu, Z., Yang, J., Zhao, L., Fan, Y.: Accurate segmentation of nuclei in pathological images via sparse

- reconstruction and deep convolutional networks. *Neurocomputing* **229**, 88–99 (2017)
39. Paramanandam, M., O Byrne, M., Ghosh, B., Mammen, J.J., Manipadam, M.T., Thamburaj, R., Pakrashi, V.: Automated segmentation of nuclei in breast cancer histopathology images. *PLoS ONE* **11**(9), e0162053 (2016)
 40. Peikari, M., Salama, S., Nofech-Mozes, S., Martel, A.L.: A cluster-then-label semi-supervised learning approach for pathology image classification. *Sci. Rep.* **8**(1), 1–13 (2018)
 41. Perona, P., Malik, J.: Scale-space and edge detection using anisotropic diffusion. *IEEE Trans. Pattern Anal. Mach. Intell.* **12**(7), 629–639 (1990)
 42. Petushi, S., Garcia, F.U., Haber, M.M., Katsinis, C., Tozeren, A.: Large-scale computations on histology images reveal grade-differentiating parameters for breast cancer. *BMC Med. Imaging* **6**(1), 14 (2006)
 43. Phung, S.L., Bouzerdoum, A.: *Visual and Audio Signal Processing Lab*. University of Wollongong, Dubai (2009)
 44. Ragothaman, S., Narasimhan, S., Basavaraj, M.G., Dewar, R.: Unsupervised segmentation of cervical cell images using Gaussian mixture model. In: *Proceedings of the IEEE Conference on Computer Vision and Pattern Recognition Workshops*, pp. 70–75 (2016)
 45. Rashwan, H.A., García, M.A., Puig, D.: Variational optical flow estimation based on stick tensor voting. *IEEE Trans. Image Process.* **22**(7), 2589–2599 (2013)
 46. Rezaeilouyeh, H., Mollahosseini, A., Mahoor, M.H.: Microscopic medical image classification framework via deep learning and shearlet transform. *J. Med. Imaging* **3**(4), 044501 (2016)
 47. Sarkar, R., Acton, S.T.: SDL: saliency-based dictionary learning framework for image similarity. *IEEE Trans. Image Process.* **27**(2), 749–763 (2018)
 48. Shaikh, T.A., Ali, R., Beg, M.S.: Transfer learning privileged information fuels cad diagnosis of breast cancer. *Mach. Vis. Appl.* **31**(1), 9 (2020)
 49. Shareef, S.R.: Breast cancer detection based on watershed transformation. *IJCSI Int. J. Comput. Sci. Issues* **11**(1), 237–245 (2014)
 50. Tata Medical Center: <https://tmckolkata.com/tmc/> (2017)
 51. Tokime, R.B., Ellassady, H., Akhloufi, M.A.: Identifying the cells' nuclei using deep learning. In: *2018 IEEE Life Sciences Conference (LSC)*, pp. 61–64. IEEE (2018)
 52. Veta, M., van Diest, P.J., Kornegoor, R., Huisman, A., Viergever, M.A., Pluim, J.P.: Automatic nuclei segmentation in H&E stained breast cancer histopathology images. *PLoS ONE* **8**(7), e70221 (2013)
 53. Veta, M., Pluim, J.P., Van Diest, P.J., Viergever, M.A.: Corrections to “breast cancer histopathology image analysis: a review” [May 14 1400–1411]. *IEEE Trans. Biomed. Eng.* **61**(11), 2819–2819 (2014)
 54. Wan, T., Cao, J., Chen, J., Qin, Z.: Automated grading of breast cancer histopathology using cascaded ensemble with combination of multi-level image features. *Neurocomputing* **229**, 34–44 (2017)
 55. Wang, L., Lu, H., Ruan, X., Yang, M.H.: Deep networks for saliency detection via local estimation and global search. In: *Proceedings of the IEEE Conference on Computer Vision and Pattern Recognition*, pp. 3183–3192 (2015)
 56. Wang, C.W., Yu, C.P.: Automated morphological classification of lung cancer subtypes using H&E tissue images. *Mach. Vis. Appl.* **24**(7), 1383–1391 (2013)
 57. Wang, P., Hu, X., Li, Y., Liu, Q., Zhu, X.: Automatic cell nuclei segmentation and classification of breast cancer histopathology images. *Signal Process.* **122**, 1–13 (2016)
 58. Wienert, S., Heim, D., Saeger, K., Stenzinger, A., Beil, M., Hufnagl, P., Dietel, M., Denkert, C., Klauschen, F.: Detection and segmentation of cell nuclei in virtual microscopy images: a minimum-model approach. *Sci. Rep.* **2**, 503 (2012)
 59. Wulandari, C.D.R., Wibowo, S.A., Novamizanti, L.: Classification of diabetic retinopathy using statistical region merging and convolutional neural network. In: *2019 IEEE Asia Pacific Conference on Wireless and Mobile (APWiMob)*, pp. 94–98. IEEE (2019)
 60. Xu, J., Janowczyk, A., Chandran, S., Madabhushi, A.: A high-throughput active contour scheme for segmentation of histopathological imagery. *Med. Image Anal.* **15**(6), 851–862 (2011)
 61. Yang, W., Chen, Y., Liu, Y., Zhong, L., Qin, G., Lu, Z., Feng, Q., Chen, W.: Cascade of multi-scale convolutional neural networks for bone suppression of chest radiographs in gradient domain. *Med. Image Anal.* **35**, 421–433 (2017)
 62. You, Y.L., Xu, W., Tannenbaum, A., Kaveh, M.: Behavioral analysis of anisotropic diffusion in image processing. *IEEE Trans. Image Process.* **5**(11), 1539–1553 (1996)
 63. Yu, C., Chen, H., Li, Y., Peng, Y., Li, J., Yang, F.: Breast cancer classification in pathological images based on hybrid features. *Multimedia Tools Appl.* **78**(15), 21325–21345 (2019)
 64. Zhao, R., Ouyang, W., Li, H., Wang, X.: Saliency detection by multi-context deep learning. In: *Proceedings of the IEEE Conference on Computer Vision and Pattern Recognition*, pp. 1265–1274 (2015)
 65. Zheng, B., Yoon, S.W., Lam, S.S.: Breast cancer diagnosis based on feature extraction using a hybrid of k-means and support vector machine algorithms. *Expert Syst. Appl.* **41**(4), 1476–1482 (2014)
 66. Zhou, Y., Chen, H., Xu, J., Dou, Q., Heng, P.A.: IRNET: instance relation network for overlapping cervical cell segmentation. In: *International Conference on Medical Image Computing and Computer-Assisted Intervention*, pp. 640–648. Springer (2019)
 67. Zhou, S.K., Greenspan, H., Shen, D.: *Deep Learning for Medical Image Analysis*. Academic Press, Cambridge (2017)



R. Krithiga is a Research Scholar in the Department of Computer Science and Engineering, College of Engineering, Guindy, Anna University, Chennai, India. Her research focuses on image processing, machine learning and deep learning.



P. Geetha is a Professor in the Department of Computer Science and Engineering, College of Engineering, Anna University, Guindy, Chennai, India. Her research focuses on image processing and pattern recognition.